

Large depth-high resolution full 3D imaging of the anterior segments of the eye using high speed Optical Frequency Domain Imaging

C. Kerbage¹, H. Lim¹, W. Sun^{1,2}, M. Mujat¹, and J.F. de Boer^{1*}

¹Wellman Center for Photomedicine, Harvard Medical School and, Massachusetts General Hospital
50 Blossom Street, Boston, Massachusetts 02114

²Boston University, Department of Physics, Boston, MA 02114

*Corresponding author: deboer@helix.mgh.harvard.edu

Abstract: Three dimensional rapid large depth range imaging of the anterior segments of the human eye by an optical frequency domain imaging system is presented. The tunable source spans from 1217 to 1356 nm with an average output power of 60 mW providing a measured axial resolution of 10 μm in air based on the coherence envelope. The effective depth range is 4 mm, defined as the distance over which the sensitivity drops by 6 dB, achieved by frequency shifting the optical signal using acousto-optic modulators. The measured maximum sensitivity is 109 dB at a sample arm power of 14.7mW and A-lines rate of 43,900 per second. Images consisting of 512 depth profiles are acquired at an acquisition rate of 85 frames per second. We demonstrate an optical frequency domain imaging system capable of mapping *in vivo* the entire area of the human anterior segment (13.4 x 12 x 4.2 mm) in 1.4 seconds.

©2007 Optical Society of America

OCIS codes: (110.4500) Optical coherence tomography; (120.3180) Interferometry; (140.3600) Lasers, tunable; (170.3880) Medical and biological imaging; (170.4470) Ophthalmology; (330.4460) Ophthalmic optics

References and links

1. D. Huang, E. A. Swanson, C. P. Lin, J. S. Schuman, W. G. Stinson, W. Chang, M. R. Hee, T. Flotte, K. Gregory, C. A. Puliafito, and J. G. Fujimoto, "Optical Coherence Tomography," *Science* **254**, 1178-1181 (1991).
2. M. R. Hee, J. A. Izatt, and E. A. Swanson, "Optical coherence tomography of the human retina," *Arch. Ophthalmol.* **113**, 325-332 (1995).
3. A. F. Fercher, C. K. Hitzenberger, W. Drexler, G. Kamp, and H. Sattmann, "In-Vivo Optical Coherence Tomography," *Am. J. Ophthalmol.* **116**, 113-115 (1993).
4. W. Drexler, U. Morgner, R. K. Ghanta, F. X. Kartner, J. S. Schuman, and J. G. Fujimoto, "Ultra-high-resolution ophthalmic optical coherence tomography," *Nat. Med.* **7**, 502-507 (2001).
5. M. R. Hee, C. R. Baumal, C. A. Puliafito, J. S. Duker, E. Reichel, J. R. Wilkins, J. G. Coker, J. S. Schuman, E. A. Swanson, and J. G. Fujimoto, "Optical coherence tomography of age-related macular degeneration and choroidal neovascularization," *Ophthalmology* **103**, 1260-1270 (1996).
6. S. Roh, R. J. Noecker, and J. S. Schuman, "Evaluation of coexisting optic nerve head drusen and glaucoma with optical coherence tomography," *Ophthalmology* **104**, 1138-1144 (1997).
7. J. A. Izatt, M. R. Hee, E. A. Swanson, C. P. Lin, D. Huang, J. S. Schuman, C.A. Puliafito, and J. G. Fujimoto, "Micrometer-scale resolution imaging of the anterior eye in vivo with optical coherence tomography," *Arch. Ophthalmol.* **112**, 1584-1589 (1994).
8. S. Radhakrishnan, A. M. Rollins, J. E. Roth, A. Yazdanfar, V. Westphal, D. Bardenstein, and J. A. Izatt, "Real-Time Optical Coherence Tomography of the Anterior Segment at 1310nm," *Arch. Ophthalmol.* **119**, 1179-1185 (2001).
9. S. Kaufman, D. Musch, M. W. Belin, E. J. Cohen, D. Meisler, W. J. Reinhart, I. J. Dell, and W. S. V. Meter, "Confocal Microscopy," *Am. Acad. Ophthalmol.* **111**, 396-406 (2003).
10. D. Z. Reinstein, R. H. Silverman, S. L. Trokel, and D. J. Coleman, "Corneal pachymetric topography," *Ophthalmology* **112**, 1584-1589 (1994).
11. A. S. Neubauer, S. G. Priglinger, M. J. Thiel, C. A. May, and U. C. Welge-Luben, "Sterile Structural Imaging of Donor Cornea by Optical Coherence Tomography," *Cornea* **21**, 490-494 (2002).

12. Y. Li, R. Shekhar, and D. Huang, "Corneal Pachymetry Mapping with High-speed Optical Coherence Tomography," *Am. Acad. Ophthalmol.* **113**, 792-799 (2006).
13. C. Wirbelauer, C. Scholz, H. Hoerauf, D. Thoai Pham, H. Laqua, and R. Birngruber, "Noncontact Corneal Pachymetry with Slit Lamp-adapted Optical Coherence Tomography," *Am. J. Ophthalmol.* **133**, 444-450 (2002).
14. V. Westphal, A. Rollins, S. Radhakrishnan, and J. A. Izatt, "Correction of geometric and refractive image distortions in optical coherence tomography applying Fermat's principle," *Opt. Express* **10**, 397-404 (2002).
15. S. Radhakrishnan, J. Goldsmith, D. Huang, V. Westphal, D. K. Dueker, A. M. Rollins, J. A. Izatt, and S. D. Smith, "Comparison of Optical Coherence Tomography and Ultrasound Biomicroscopy for Detection of Narrow Anterior Chamber Angles," *Arch. Ophthalmol.* **123**, 1053-1059 (2005).
16. S. Muscat, N. McKay, S. Parks, E. Kemp, and D. Keating, "Repeatability and Reproducibility of Corneal Thickness Measurements by Optical Coherence Tomography," *Invest. Ophthalmol. Visual Sci.* **43**, 1791-1795 (2002).
17. M. J. Maldonado, L. Ruiz Oblitas, J. M. Munuera, D. Aliseda, A. Garcia-Layana, and J. Moreno-Montanes, "Optical Coherence Tomography evaluation of the corneal cap and stromal bed features after laser in situ keratomileusis for high myopia and astigmatism," *Ophthalmology* **107**, 81-87 (2000).
18. G. Geerling, M. Muller, C. Winter, H. Hoerauf, S. Oelckers, and R. Birngtuber, "Intraoperative 2-Dimensional Optical Coherence Tomography as a New Tool for Anterior Segment Surgery," *Arch. Ophthalmol.* **123**, 253-257 (2005).
19. M. Wojtkowski, R. Leitgeb, A. Kowalczyk, T. Bajraszewski, and A. F. Fercher, "In vivo human retinal imaging by Fourier domain optical coherence tomography," *J. Biomed. Opt.* **7**, 457-463 (2002).
20. N. Nassif, B. Cense, B. H. Park, S. H. Yun, T. C. Chen, B. E. Bouma, G. J. Tearney, and J. F. de Boer, "In vivo human retinal imaging by ultrahigh-speed spectral domain optical coherence tomography," *Opt. Lett.* **29**, 480-482 (2004).
21. S. H. Yun, G. J. Tearney, B. E. Bouma, B. H. Park, and J. F. de Boer, "High-speed spectral-domain optical coherence tomography at 1.3 μ m wavelength," *Opt. Express* **11**, 3598-3604 (2003).
22. R. Leitgeb, C. K. Hitzenberger, and A. F. Fercher, "Performance of fourier domain vs. time domain optical coherence tomography," *Opt. Express* **11**, 889-894 (2003).
23. J. F. de Boer, B. Cense, B. H. Park, M. C. Pierce, G. J. Tearney, and B. E. Bouma, "Improved signal-to-noise ratio in spectral-domain compared with time-domain optical coherence tomography," *Opt. Lett.* **28**, 2067-2069 (2003).
24. W. Drexler, H. Sattmann, B. Hermann, T. H. Ko, M. Stur, A. Unterhuber, C. Scholda, O. Findl, M. Wirtitsch, J. G. Fujimoto, and A.F. Fercher, "Enhanced visualization of macular pathology with the use of ultrahigh-resolution optical coherence tomography," *Archives of Ophthalmology* **121**, 695-706 (2003).
25. M. A. Choma, M. V. Sarunic, C. H. Yang, and J. A. Izatt, "Sensitivity advantage of swept source and Fourier domain optical coherence tomography," *Opt. Express* **11**, 2183-2189 (2003).
26. S. H. Yun, G. J. Tearney, J. F. de Boer, N. Ifimia, and B.E. Bouma, "High-speed optical frequency-domain imaging," *Opt. Express* **11**, 2593-2963 (2003).
27. S. H. Yun, C. Boudoux, G. J. Tearney, and B. E. Bouma, "High-speed wavelength-swept source semiconductor laser with a polygon-scanner-based wavelength filter," *Opt. Lett.* **28**, 1981-1983 (2003).
28. S. R. Chinn, E. A. Swanson, and J. G. Fujimoto, "Optical coherence tomography using a frequency tunable optical source," *Opt. Lett.* **22**, 340-342 (1997).
29. B. J. Vakoc, S. H. Yun, J. F. de Boer, G. J. Tearney, and B.E. Bouma, "Phase-resolved optical frequency domain imaging," *Opt. Express* **13**, 5483-5493 (2005).
30. S. H. Yun, G. J. Tearney, J. F. de Boer, and B. E. Bouma, "Removing the depth-degeneracy in optical frequency domain imaging with frequency shifting," *Opt. Express* **12**, 4822-4828 (2004).
31. W. Y. Oh, S. H. Yun, G. J. Tearney, and B. E. Bouma, "115 kHz tuning repetition rate ultrahigh-speed wavelength-swept semiconductor laser," *Opt. Lett.* **30**, 3159-3161 (2005).
32. R. Huber, M. Wojtkowski, and J. G. Fujimoto, "Fourier Domain Mode Locking (FDML): A new laser operating regime and applications for optical coherence tomography," *Opt. Express* **14**, 3225-3237 (2006).
33. E. C. W. Lee, J. F. de Boer, M. Mujat, H. Lim, and S.H. Yun, "In vivo optical frequency domain imaging of human retina and choroid," *Opt. Express* **14**, 4403-4411 (2006).
34. H. Lim, J. F. de Boer, B. H. Park, E. C. Lee, R. Yelin, and S. H. Yun, "Optical frequency domain imaging with a rapidly swept laser in the 815-870nm range," *Opt. Express* **14**, 5937-5944 (2006).
35. H. Lim, M. Mujat, C. Kerbage, E. C. Lee, Y. Chen, T. C. Chen, and J. F. de Boer, "High-speed imaging of human retina in vivo with swept source optical coherence tomography," *Opt. Express* **14**, 12902-12908 (2006).
36. M. V. Sarunic, M. A. Choma, C. Yang, and J. A. Izatt, "Instantaneous complex conjugate resolved spectral domain and swept-source OCT using 3by3 couplers," *Opt. Express* **13**, 957-967 (2005).
37. Y. Yasuno, V. D. Madjarova, S. Makita, M. Akiba, A. Morosawa, C. Chong, T. Sakai, K. P. Chan, M. Itoh, and T. Yatagai, "Three dimensional and high-speed swept-source optical coherence tomography for in vivo investigation of human anterior eye segments," *Opt. Express* **13**, 10652-10664 (2005).

38. Y. Yasuno, M. Yamanari, H. Mori, K. Kawana, Y. Watanabe, M. Miura, A. Miyazawa, T. Oshika, and T. Yatagai, "Clinical examinations of anterior eye segments by three-dimensional swept-source optical coherence tomography," *Proc. SPIE* **6426**, 64260U (2007).
 39. J. W. McLaren, C. B. Nau, J. C. Erie, and W. M. Bourne, "Corneal thickness measurement by confocal microscopy, ultrasound, and scanning slit method," *Am. J. Ophthalmol.* **137**, 1011-1020 (2004).
 40. S. Haque, T. Simpson, and L. Jones, "Corneal and Epithelial thickness in Keratoconus: A comparison of Ultrasonic Pachymetry, Obscan II, and Optical Coherence Tomography," *J. Refractive Surgery* **22**, (2006).
 41. G. R. Melles, F. Lander, F. J. Rietveld, L. Remeijer, and W. H. Beekhuis, "A new surgical technique for deep stromal, anterior lamellar keratoplasty," *Br. J. Ophthalmol.* **83**, 327-333 (1999).
 42. N. Nassif, B. Cense, B. H. Park, M. Pierce, S. H. Yun, B. Bouma, G. Tearney, T. Chen, and J. F. de Boer, "In vivo high-resolution video-rate spectral domain optical coherence tomography," *Opt. Express* **12**, (2004).
 43. G. Hausler and M. W. Linder, "Coherence Radar and Spectral Radar- new tools for dermatological diagnosis," *J. Biomed. Opt.* **3**, 21-31 (1998).
-

1. Introduction

Optical coherence tomography (OCT) has been established as a powerful imaging technique capable of detecting micro-meter scale features of biological samples using low coherence interferometry [1]. Imaging the eye with OCT is being widely developed for its non contact and non-invasive capabilities to generate high resolution cross sectional images [2-4]. Ophthalmic OCT was first developed for imaging the posterior segments for quantitative evaluation of vitreo-retinal diseases of the macula [5] and optic disk [6]. The application of OCT to image the anterior segments (AS) of the eye, specifically the cornea, was first reported by Izatt *et al.* using a time domain OCT system (TD-OCT) with a superluminescence diode source at 800 nm [7]. Light sources centered at 1.3 μm were later implemented since this longer wavelength provides better penetration through scattering tissue like sclera to better visualize the ciliary body and because the maximum permissible power into the eye is significantly higher due to the stronger absorption of this wavelength by the vitreous leading to a better signal to noise ratio (SNR) [8].

Recent clinical studies have investigated imaging of the anterior segments with OCT, complementing or potentially replacing other commercially available imaging techniques such as confocal microscopy [9] and ultrasonic bio-microscopy [10]. OCT has been demonstrated as an objective tool in corneal structural imaging[11], corneal pachymetry [12, 13], detection of narrow anterior chamber angles [14, 15], and measurement of corneal thickness [16], as well as in post operative evaluation of LASIK surgery[17], and intra-operative diagnostic in anterior segment surgery [18].

The introduction of spectral domain OCT (SD-OCT) has provided several orders of magnitude improvement in sensitivity over conventional or TD-OCT, permitting a hundred fold improvement in speed and addressing the need for high speed imaging to reduce motion artifacts [19-24]. An equivalent technology, Optical Frequency Domain Imaging (OFDI), employs a rapidly tuned laser to measure the wavelength resolved interference and provides similar sensitivity advantage as SD-OCT over TD-OCT [3, 25-28]. Most advances in OFDI were demonstrated in the 1.3 μm wavelength region such as phase resolved [29], degeneracy removal[30], and speed with A-line rates exceeding 100 kHz [31, 32]. Recently, OFDI systems with different cavity configurations have been developed at wavelengths of 1050 nm [33] and 800 nm [34] and were successfully applied to visualize the posterior segments of the human eye [33, 35].

Although several studies for imaging the anterior segments of the eye using OFDI have been reported, a sweep rate of 250 Hz [36] or a sensitivity drop of 6 dB over 1.07 mm [37] or 1.67 mm [38] are insufficient to rapidly image the complete anterior segment in a clinical setting.

In this paper, we present an OFDI system that is capable of obtaining full thickness images of the sclera, angle and iris with a 43.9 KHz A-line rate, acquiring 85 frames per

second. A sensitivity drop of 6 dB over a depth range of 4 mm was achieved by frequency shifting the detector signal to double the ranging depth. 3-D visualization of the cornea has several advantages over spot measurement techniques [39], that deal just with the center of the cornea, and provides valuable information for the evaluation of abnormal patterns such as keratoconus [40] and in preoperative diagnostics such as lamellar keratoplasty [41].

2. System setup and characterization

A schematic diagram of the circular cavity design source centered at 1290nm and tunable filter that was described earlier is shown in Fig. 1 [26]. In the circular cavity, the gain medium is a custom, bi-directional semiconductor optical amplifier with a small signal gain of 30 dB and a ASE -3dB bandwidth of 79.6 nm at an injection current of 600 mA (Covega Inc.). The output of the amplifier is connected to a 2x2 fiber coupler that couples 50% of the intra-cavity power to an interferometer. The remaining 50% is connected to a circulator that couples to a wavelength-scanning filter. The tunable filter is composed of a diffraction grating (830 lines/mm), a telescopic lens pair ($F_1 = 75$ mm, $F_2 = 50$ mm), and a polygon mirror scanner (Lincoln Lasers, Inc., 72 facets). Light from a fiber optic collimator ($f=11$ mm) is incident on the grating at an angle of about 60 degrees and diffracted onto the lens pair.

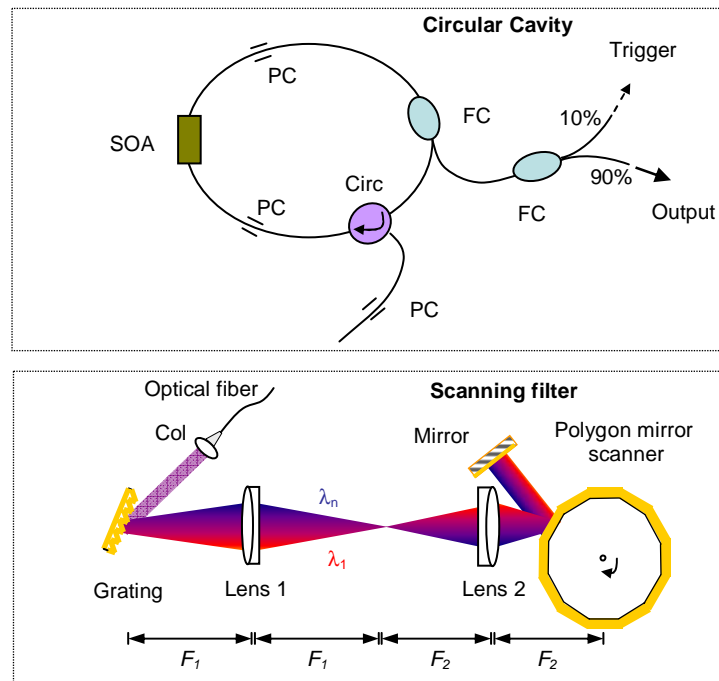


Fig. 1. Schematic diagram of the tunable source consists of a scanning filter and a circular cavity. SOA: semiconductor optical amplifier; PC: polarization controller; Circ: Circulator; Col: collimator; FC: fiber coupler. A 12-sided polygon instead of 72-sided one utilized in the experiment is illustrated in the figure.

By positioning the scanner off axis and placing a mirror as an end reflector, the scan angle can be doubled, doubling the free spectral range of the source [31]. The filter was designed to give a line-width of ~ 0.18 nm and a free spectral range of 140 nm. On the return path from the tunable filter, light couples back to the gain medium and gets amplified.

The output of the tunable source is shown in Fig. 2(a), recorded with an optical spectrum analyzer in peak hold mode at 0.1 nm resolution. The tuning rate was set at 43.9 KHz,

resulting in an average output power of 60 mW with the SOA driven at an injection current of 800 mA. The laser spectrum spans from 1217 to 1356 nm with a Full Width at Half Maximum (FWHM) of 135 nm. The time response of the laser output is shown in Fig. 2(b) over six wavelength sweeps measured with an oscilloscope.

A trigger signal is generated by tapping 10% of the output light that is passed through a narrow band filter, consisting of a fiber Bragg grating and a circulator, to a photo-detector (Newfocus Inc.) that detects a train of short pulses generated when the output spectrum of the laser swept through the pass band (center wavelength 1300 nm and bandwidth 0.16 nm) of the filter. TTL pulsed are then generated from the photo-detector output using a tunable trigger delay circuit. The remainder of the output light (90%) is split into the two arms of an interferometer by a 10/90 fiber coupler where 90% of the light is coupled into the sample arm.

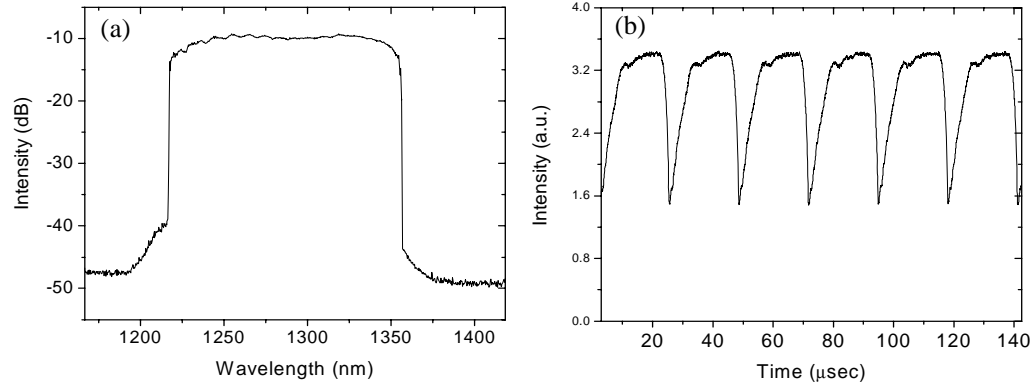


Fig. 2. (a). Measured spectrum of the output laser cavity with a bandwidth of 135nm in peak hold mode (b) Time response of the laser showing six wavelengths sweeps.

The depth range of the OFDI system is doubled by introducing a carrier frequency shift by means of Acousto-Optic Modulators (AOMs, Brimrose Inc.) in both the sample and reference arms. In the current system, the two AOMs (Brimrose Corp.) at $f_1 = 76$ MHz and $f_2 = 55$ MHz set at 1st order diffraction produce a net frequency shift $\Delta f = |(f_1 - f_2)| = 21$ MHz in the interference signal. The signals are then directed by optical fiber circulators (AC Photonics Inc.) to the eye (sample arm) and a mirror (reference arm). Light reflected from the sample and mirror is combined using a 50/50 fiber coupler and the interference signal is detected by an InGaAs dual-balanced detector (New Focus Inc.). The detector signal was further amplified by a low pass (100 MHz) voltage amplifier (Femto, Germany) with a 20 dB gain.

The intensity of the interference signal detected is expressed by

$$I(t) \propto A\sqrt{S_s S_r} \int \cos[2Kz + 2\pi\Delta ft + \phi(z)] \quad (1)$$

where S_s and S_r are the sample and reference arm power, respectively, $\phi(z)$ is the phase of the backscattered light, and Δf is the phase shift introduced by the AOMs.

The scanning mechanism is installed on a modified slit lamp to accommodate a collimator ($f=16$ mm), a pair of galvanometer mirrors and a lens of focal length 150 mm producing a beam diameter of 62 μ m with a Rayleigh range of 2.6 mm on the cornea.

Data is acquired and digitized by a data acquisition board (National Instruments, PCI-5124) and digitized at a sampling rate of 100Msamples/second. Post-processing of the data is performed by obtaining the mean of the depth profiles, interpolating the data points evenly in k-space, compensating for dispersion in the system and performing fast Fourier transformation; all of these processes have been described previously in details [42].

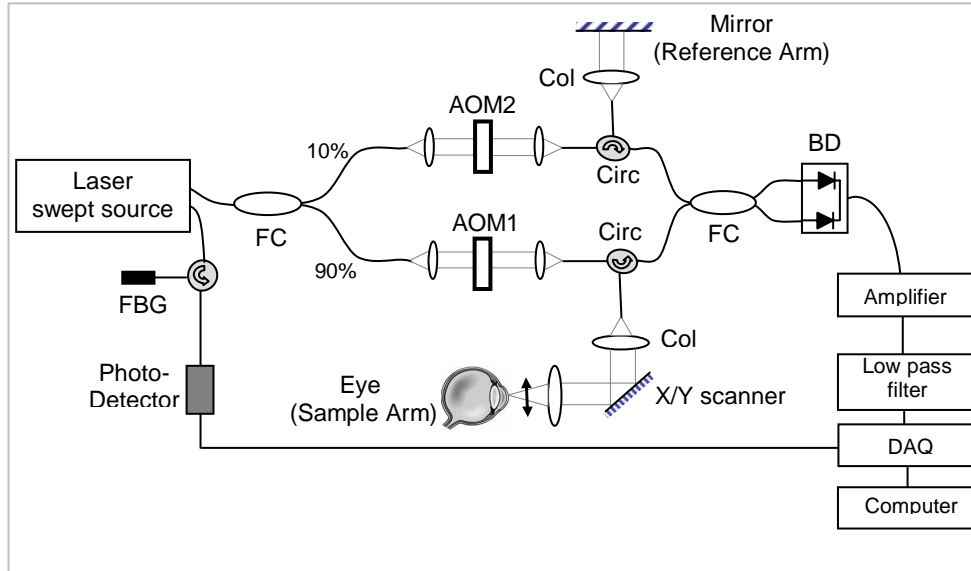


Fig. 3. Schematic diagram of the OFDI system set for imaging the anterior segments. Two AOMs are introduced into the sample and reference arms to obtain a net frequency shift of 21MHz. Circ: fiber circulator; Col: collimator; FBG: fiber Bragg grating; BD: balanced detector; FC: fiber coupler.

The system performance was characterized by placing a partial reflector with a measured attenuation of -53 dB in the sample arm and measuring the axial point spread function as a function of depth (Fig. 4). The depth range in air, $\Delta z = \lambda_0^2 / 4\delta\lambda$ [43], is determined by the laser line width, $\delta\lambda$, and the center wavelength, λ_0 , of the source. Introducing a constant shift of the signal, as described in a previous work [30], the zero signal frequency is shifted to a positive depth and results in doubling the imaging depth range. The depth at which the signal drops by 6 dB, represented by a dashed line in Fig. 4, is measured to be about 2 mm on each side of the zero optical delay location, which is in agreement with the theoretical designed values, giving an effective imaging range of 4 mm. The total imaging range, defined by the sweep rate, tuning range and detection bandwidth (50 MHz) is 6.8 mm. The measured axial resolution of the system is approximately 7 μm in tissue ($n=1.4$) measured at the -6 dB points on intensity peak or equivalently the -3 dB point of the coherence envelope. The resolution defined by the -3 dB points on the intensity peak resulted in a resolution of 8.6 μm in air or ~ 6 μm in tissue. The full width half maximum of the peak is constant along the entire depth range. The optimal reference arm power is determined to be about 20 μWatt by measuring the signal to noise ratio as a function of reference arm power. The theoretical shot noise limit is calculated to be about 119 dB from the following equation: Sensitivity (dB) = $-10 \log(\eta P_s / h\nu f_A)$, where f_A is the A-line rate, $h\nu$ is the energy of a photon, η (=0.85%) is the detector efficiency and P_s is the power of the sample arm returning to the detector (6.7 mW) measured by placing a mirror in the sample arm. The power in the sample arm was 14.7 mW. The measured SNR of the system is about 109 dB at zero delay pointed to by an arrow in Fig. 4 (which corresponds to the carrier frequency, f_c), based in a measured 55.9 dB SNR of the peak and an attenuation in the sample arm of -53.5 dB, and 103 dB at 2 mm depth range. The side-lobes observed on both sides of the main mirror peaks are the results of residual spectral modulation in the light source. Since the intensity of the side-lobes is 40dB below that of the

maximum of the main peaks, they have no effect on the image quality especially in our case where the dynamic range of the images is about 40 dB as mentioned below.

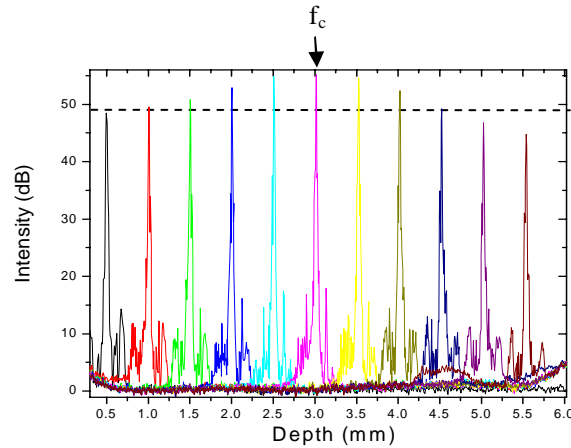


Fig. 4. Axial point spread function of a partial reflector placed in the sample arm at different depth locations. An intensity drop of 6dB at ~2mm (dashed line) is measured on each side of the coherence function (in air).

4. Results

Anterior segments images of the right eye of a healthy volunteer were obtained with the OFDI system. A series of images of 512 depth points each were continuously acquired at 43,900 A-lines per second resulting in an acquisition rate of 85 frames per second. Each frame image in Fig. 5(a) is cropped to 490 depth profiles to span an area 13.4 mm wide horizontally across the cornea by 4.2 mm in depth. The slow axis scanned vertically over 12 mm in 1.4 sec

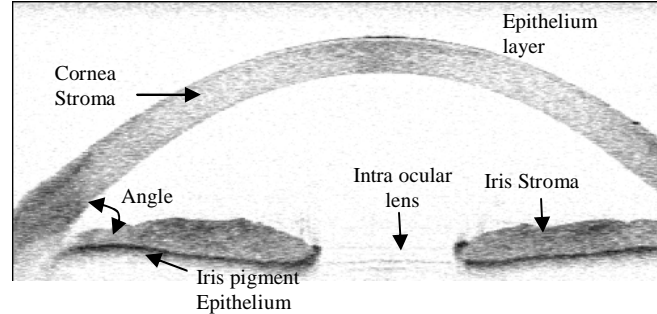


Fig. 5. (3.58 MB) Sequence of 120 images of the cornea anterior segments of the right eye of a healthy volunteer. Each image frame consists of 490 depth profiles and spans a horizontal range of 13.4mm along horizontal (x-axis) and 4.15mm in depth along a vertical scan of 12mm. Total of 120 frames were acquired in 1.4 seconds.

The images are shown at a rate of 5 frames per second with an inverse logarithmic gray scale mapping with an average reflectivity dynamic range of 45 dB. The intensity of light directed to the slit lamp measured after the collimator is 14.7mW which is below the limit set by the American National Standards Institute. Full thickness images visualizing the corneal stroma, epithelium layer, sclera, angle and iris stroma were acquired.

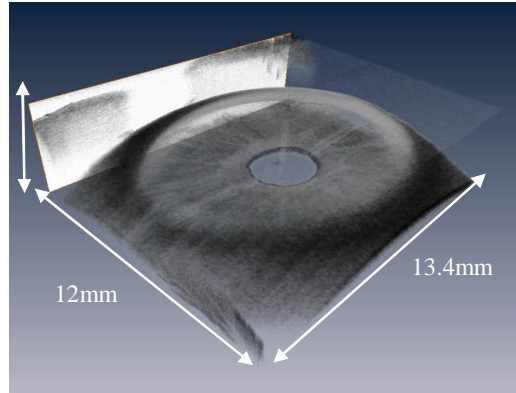


Fig. 6. (6.67 MB) Three dimensional tomography of the anterior segment of the human eye. The volume consist of 490x120x840 pixels spans a volume of $(13.4 \times 12 \times 4.1) \text{mm}^3$.

Figure 6 is a 3-dimensional rendering of the full structure of the anterior segment of a human eye reconstructed from a series of *in vivo* cross-sectional images (Fig. 5) using a commercial 3D visualization software (*Amira*). The 3D image spans an area of 13.4 mm by 12 mm and height 4.1 mm. The OFDI cornea images demonstrate the large depth range that is achieved and can be valuable in providing 3-D structural information. For example, open angle glaucoma, corneal thickness and corneal changes of its shape after refractive surgery can be detected.

Imaging of the anatomical structures of the anterior segments such as the cornea and ciliary body was performed after increasing the lateral resolution by reconfiguring the focusing lens to obtain a beam waist of $40 \mu\text{m}$ on the cornea. The depth of focus in this case is calculated to be 1.3 mm. Figure 7 is a series of images showing (a) corneal layers and (b) anatomical features of the angular structures such as sclera, ciliary body, and the trabecular meshwork. Figure 7(c) is the corresponding 3D rendering showing the angle of the right eye of a human volunteer. The movie presented is constructed from 60 frames with 1024 A-lines acquired at 43.9 KHz in 1.4 sec. The region scanned is 5 by 5 mm.

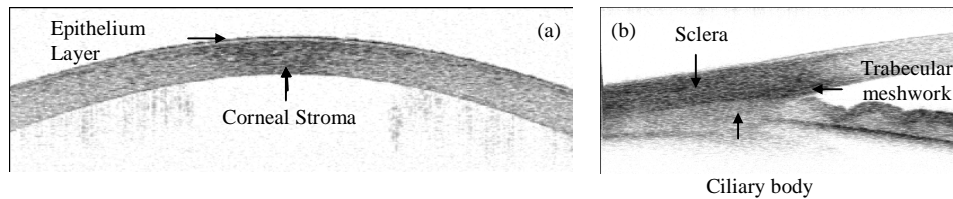


Fig. 7. (1.81 MB) Sequence of 60 images of the (a) cornea and (b) angle structures of the right eye of a human volunteer. Each image consists of 1024 depth profiles acquired at a frame rate of 43 frames per second.

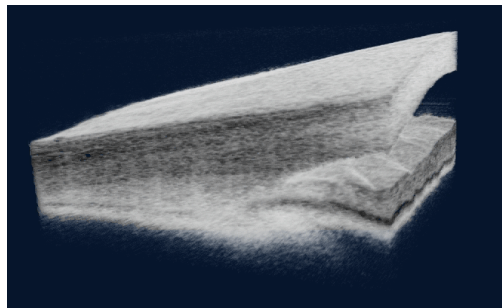


Fig. 7. (c). (8.49 MB) Three dimensional tomography of the angle section of the right eye of a human volunteer. The movie is constructed from 60 frames each consist of 1024 depth profiles. The movie consists of 848x704x60 pixels and spans a volume (5x3.6x5) mm³ of the angle.

5. Summary

We demonstrate an OFDI system with large depth and high speed that is capable to obtain full *in-vivo* 3D images of the entire anterior segments of the human eye. Cross sectional images are obtained at a rate of up to 85 frames per second, with axial resolution 7 μm in tissue and dynamic range of 45 dB. The current system can provide precise and objective information about ocular pathologies and surgical anatomy of the anterior segments of the eye. In particular, due to the superior depth range of > 4 mm, its speed and ability to map the entirety of the anterior and posterior surface of the cornea as well as the elevation of the actual surface, and the overall shape and the macro-irregularities of the corneal surface (e.g. corneal astigmatism), OFDI is ideally suited for clinical applications. Moreover, the imaging system can detect changes in the 3-D structure and opacity of the cornea which is important especially in the case of injuries (abrasions, infections) or refractive surgery, as for example, to visualize the LASIK flap. Examination of the cornea can also be useful for preoperative assessment, determining the amount of correction, and subsequently analyzing the effectiveness of the procedure and biomechanical changes post surgery.

Acknowledgments

This research was supported in part by research grants from the National Institutes of Health (R01 RR019768 R01 EY014975) and the Department of Defense (F4 9620-01-1-0014).